ADVANCED MATERIALS
www.advmat.de

Tuning the Structural and Optoelectronic Properties of $Cs_2AgBiBr_6$ Double-Perovskite Single Crystals through Alkali-Metal Substitution

Masoumeh Keshavarz,* Elke Debroye,* Martin Ottesen, Cristina Martin, Heng Zhang, Eduard Fron, Robert Küchler, Julian A. Steele, Martin Bremholm, Joris Van de Vondel, Hai I. Wang, Mischa Bonn, Maarten B. J. Roeffaers, Steffen Wiedmann, and Johan Hofkens*

Lead-free double perovskites have great potential as stable and nontoxic optoelectronic materials. Recently, $Cs_2AgBiBr_6$ has emerged as a promising material, with suboptimal photon-to-charge carrier conversion efficiency, yet well suited for high-energy photon-detection applications. Here, the optoelectronic and structural properties of pure $Cs_2AgBiBr_6$ and alkali-metal-substituted $(Cs_{1-x}Y_x)_2AgBiBr_6$ (Y: Rb^+, K^+, Na^+; x = **0.02**) single crystals are investigated. Strikingly, alkali-substitution entails a tunability to the material system in its response to X-rays and structural properties that is most strongly revealed in Rb-substituted compounds whose X-ray sensitivity outperforms other double-perovskite-based devices reported. While the fundamental nature and magnitude of the bandgap remains unchanged, the alkali-substituted materials exhibit a threefold boost in their fundamental carrier recombination lifetime at room temperature. Moreover, an enhanced electron–acoustic phonon scattering is found compared to $Cs_2AgBiBr_6$. The study thus paves the way for employing cation substitution to tune the properties of double perovskites toward a new material platform for optoelectronics.

The discovery of lead-based organic-inorganic perovskite materials for optoelectronic applications has triggered a revolution in photovoltaic material research. Despite their exceptional material properties such as strong light absorption, long charge carrier lifetimes in combination with high carrier mobility, and low production costs, their long-term instability, and the toxicity of lead currently hamper their deployment at an industrial scale.[1] To overcome this drawback, double perovskites with the general formula $A_2^{1+}M^{1+}M'^{3+}X_6$ have been proposed as candidate materials providing lead-free alternatives in the vastly expanding research field of perovskites. One of the first materials investigated in this branch of the perovskite catalog is $Cs_2AgBiBr_6$, demonstrating high stability in devices[2,3] and low effective carrier masses[4] with the long carrier recombination lifetimes

Dr. M. Keshavarz, Dr. E. Debroye, Dr. C. Martin, Dr. E. Fron, Prof. J. Hofkens
Molecular Imaging and Photonics
Department of Chemistry
KU Leuven
Celestijnenlaan 200F, Leuven 3001, Belgium
E-mail: masoumeh.keshavarz@kuleuven.be; elke.debroye@kuleuven.be; johan.hofkens@kuleuven.be

Dr. M. Ottesen, Dr. M. Bremholm
Department of Chemistry and iNANO
Aarhus University
Langelandsgade 140, Aarhus C 8000, Denmark

Dr. C. Martin
Departamento de Química Física, Facultad de Farmacia de Albacete
UCLM
Albacete 02071, Spain

The ORCID identification number(s) for the author(s) of this article can be found under https://doi.org/10.1002/adma.202001878.

DOI: **10.1002**/adma.**202001878**

H. Zhang, Dr. H. I. Wang, Prof. M. Bonn, Prof. J. Hofkens
Max Planck Institute for Polymer Research
Ackermannweg 10, Mainz 55128, Germany

Dr. R. Küchler
Max Planck Institute for Chemical Physics of Solids
Nöthnitzer Str. 40, Dresden 01187, Germany

Dr. J. A. Steele, Dr. M. B. J. Roeffaers
cMACS
Department of Microbial and Molecular Systems
KU Leuven
Celestijnenlaan 200F, Leuven 3001, Belgium

Prof. J. Van de Vondel
Quantum Solid-State Physics (QSP)
Department of Physics and Astronomy
KU Leuven
Celestijnenlaan 200D, Leuven 3001, Belgium

Dr. S. Wiedmann
High Field Magnet Laboratory and Institute for Molecules and Materials
Radboud University
Toernooiveld 7, Nijmegen 6525 ED, Netherlands

Table 1. Summary of the properties of alkali-substituted $(Cs_{1-x}Y_x)_2AgBiBr_6$. X-ray response at 300 K compared to $Cs_2AgBiBr_6$, bandgap E_g at 300 and 77 K, fundamental recombination lifetime τ_4 at 300 K, electron–phonon coupling constants, Γ_0, γ_A, γ_{LO} at 250 K, phase transition temperature T^p, Debye temperature Θ_D, and THz mobility $\mu_{thin\text{-}film}$ at 300 K.

	$Cs_2AgBiBr_6$	$(Cs_{0.98}Rb_{0.02})_2AgBiBr_6$	$(Cs_{0.98}K_{0.02})_2AgBiBr_6$	$(Cs_{0.98}Na_{0.02})_2AgBiBr_6$
X-ray response at V_b = 20 V	1	4.5	0.5	0.1
E_g (300 K) [eV]	(1.79 ± 0.02)	(1.86 ± 0.10)	(1.75 ± 0.10)	(1.83 ± 0.08)
E_g (4.2 K) [eV]	1.98	1.97	1.95	1.97
Lifetime (τ_4 = 300 K) [ns]	550	1000	1500	1500
Γ_0 [meV]	155 ± 3	160 ± 2	168 ± 1	161 ± 3
γ_A [μeV K^{-1}]	186 ± 45	310 ± 30	300 ± 30	270 ± 44
γ_{LO} [meV K^{-1}]	229 ± 10	235 ± 12	225 ± 10	220 ± 20
T^p [K]	122.4	127.2	122.1	124.5
Θ_D [K]	110	75	70	60
$\mu_{thin\text{-}film}$ (300 K) [cm^2 V^{-1} s^{-1}]	≈30	≈30	≈15	≈15

exceeding 1 μs at room temperature.[5] With a variety of interesting physical properties being substantially distinct from Pb-based counterparts, $Cs_2AgBiBr_6$ has become a model system heavily under study.[6–10]

With limited promise for applications in solar cells, the first $Cs_2AgBiBr_6$-based photodetectors have displayed excellent performance when used as sensitive X-ray photodetectors at room temperature[11] and with even superior operational performance at liquid nitrogen temperature.[8] Lately, a prototype X-ray imaging flat panel detector has been fabricated based on polycrystalline $Cs_2AgBiBr_6$ wafers[12] having the potential to serve as a direct X-ray detector in a wide range of high-energy photodetection applications, in particular, for medical imaging with an extremely low detection limit (59.7 nGy s^{-1}).[11] In line with the search for highly sensitive materials to X-ray photons and to overcome the abovementioned drawbacks of lead-based perovskites, double-perovskite engineering through atomic substitution, in particular in the case of $Cs_2AgBiBr_6$ with all lattice sites available for substitution, has not yet been explored.

Atomic substitution affects the material's geometric stability through a distortion of the crystal structure in terms of constituent ionic packing,[13,14] as quantified by the Goldschmidt tolerance factor. Previous work on lead-based perovskites has shown, however, that the addition of Rb^+ and Cs^+ leads to increased stability, via homogenizing the halide distribution.[15–20] Other papers reported the improvement of both the efficiency and stability of perovskite devices via K^+-addition.[21,22] Yet, the exact underlying mechanisms giving rise to superior material properties, including efficiency, and stability upon alkali addition have been challenged by recent solid-state NMR experiments demonstrating segregation of Rb^+ and K^+ in lead-based perovskite films upon doping.[23]

In this work, we have substituted 2% of the cation Cs^+ in $Cs_2AgBiBr_6$ by the alkali metals sodium (Na^+), potassium (K^+), and rubidium (Rb^+), and investigated all compounds by an ensemble of optical, structural and electronic measurements to determine potential changes in the alkali-substituted compounds compared to $Cs_2AgBiBr_6$. The main results are summarized in Table 1. Rb-substituted $Cs_2AgBiBr_6$ is found to exhibit a substantial increase in the response to X-rays and is thus a superior candidate to replace the mother compound in X-ray detectors. The effect of alkalis has been explored via photo-physical and structural techniques down to liquid helium temperature using steady and transient photoluminescence (PL), ultrafast terahertz (THz) spectroscopy, thermal expansion and powder X-ray diffraction (PXRD). The temperature dependence of the optical and acoustic electron–phonon coupling mechanisms is extracted from the PL spectra revealing enhanced acoustic phonon scattering for the alkali-substituted crystals. We also demonstrate that 2% alkali substitution alters the structural phase transition temperatures between the high-temperature cubic and low-temperature tetragonal phase by a few degrees kelvin.

For this study, mm-sized single crystals with a thickness of 2 mm were prepared via controlled cooling,[5] for details see Experimental Section. In general, we note that alkali alloying repetitively promotes the formation of bigger crystals with well-defined morphology. Optical images of the samples are shown in Figure 1a. To correctly assess the substitution ratio, the elemental composition has been determined by inductively coupled plasma optical emission spectrometry revealing a 1.5% to 2.5% substitution of the Cs^+ ion for CsRb, CsK, and CsNa samples, respectively. Within the error bars, we refer to all compounds as $(Cs_{0.98}Y_{0.02})_2AgBiBr_6$ (Y = Rb^+, K^+, Na^+) from now on and the following abbreviations are used, Cs for the mother compound, Rb for Rb^+, K for the K^+, and Na for the Na^+ substitution, respectively. The X-ray diffraction pattern analysis for all compounds at 300 and 100 K is described in the Supporting information and illustrated in Figure 4a,b and Figure S1, Supporting Information. No change in the cubic crystal structure (space group Fm-3m (225)) is found in contrast to the alkali-doped lead-based perovskites.[16–20]

We first focus on the response of all compounds to X-ray exposure. The simulated attenuation spectra of all compounds are represented in Figure S2, Supporting Information over a broad range of photon energies indicating no significant changes upon alkali substitution. In Figure 1b, the photocurrent density at a bias of 20 V as a function of time is presented for all materials at 300 K and a 10.8 mGy s^{-1} X-rays dose rate. All devices have been exposed to X-rays for 60 s at an energy of 70 keV. Two main observations are made: i) Rb-based devices exhibit by far the highest photocurrent density, which

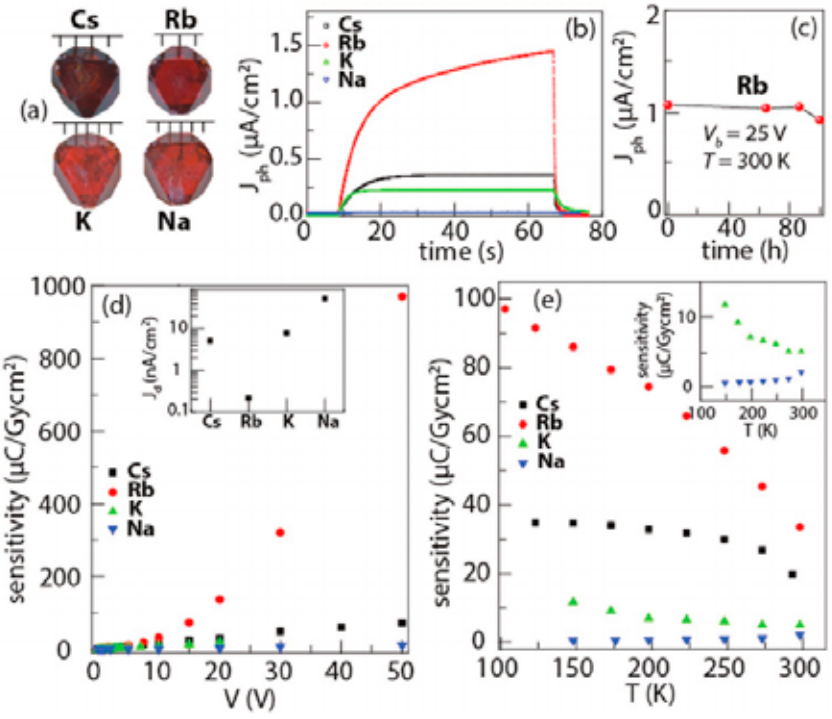

Figure 1. Bias- and temperature-dependent response of alkali-substituted $(Cs_{1-x}Y_x)_2AgBiBr_6$ and $Cs_2AgBiBr_6$ to X-ray exposure. a) Optical images of the millimeter-sized single crystals Cs, Rb, K, and Na. b) Relative response at a bias of 20 V as a function of time for all materials at 300 K: Rb devices exhibit the highest photocurrent density. c) Example for the stability of the photocurrent for Rb at 25 V bias and 300 K: just a 10% drop in the photocurrent is found measuring X-ray response after 100 h. d) Sensitivity obtained under different bias for Cs, Rb, K, and Na as a function of applied bias at 300 K. inset: dark current density for all materials at 20 V bias. e) Temperature-dependent sensitivity of all materials down to 100 K: an enhanced response (higher sensitivity) is found for all devices except for Na with decreasing temperature.

does not reach its saturation value at 60 s, and ii), except for Rb, the relative response is increasing with increasing atomic number (Na^+, K^+, Cs^+) and saturation is reached after a few seconds. The stability of the photocurrent density under a dose rate of 274.9 μGy s^{-1} for Rb at 25 V bias and at 300 K has also been measured for different time intervals and no significant decrease of the photocurrent (10% drop) is found after 100 hours indicating the device stability over time, see Figure 1c. Next, the sensitivity of the devices in units of (μC Gy^{-1} cm^{-2}) is investigated under different bias and constant dose rate (10.8 mGy s^{-1}), see Figure 1d. In the inset, a semi-log plot of the dark current for all materials prior to X-ray exposure at 20 V bias is illustrated, showing that Rb has by far the lowest dark current beneficial for X-ray detectors while the dark current for Na is enhanced by an order of magnitude compared to Cs. The temperature-dependent sensitivity for all compounds under 10 V bias, a relatively low bias, and a 10.8 mGy s^{-1} dose rate in the temperature range between 100 and 300 K relevant for applications is represented in Figure 1e. Except for Na, where a slight decrease in X-ray sensitivity is found with decreasing temperature (inset to Figure 1f), an enhanced sensitivity is observed for all devices (Experimental Section) with decreasing temperature. In fact, at 100 K, the X-ray sensitivity has more than doubled for Rb. The gain factor and photocurrent versus X-ray dose rate for Rb is illustrated in Figure S3, Supporting Information.

Considering the material properties important for X-ray detection, we are able to address three parameters here: 1) the absorption of X-rays at constant energy, 2) the generation of electron–hole pairs and 3) charge transport. In X-ray absorption, the absorption coefficient, α_X, (proportional to Z_{eff}^4 with Z_{eff} the effective atomic number) plays the fundamental role. In our systems, a 2% alkali substitution has no effect in the energy range of X-rays used for this study (50–100 keV), see Figure S2, Supporting Information. The other two parameters are related to the charge carriers in the systems: the $\mu\tau$-product with μ the carrier mobility and τ the fundamental carrier lifetime and the dark current, which should be as low as possible in the devices. From these considerations, taking into account the measured values of the dark current for all devices, the carrier mobility from THz photoconductivity experiments and the enhanced fundamental carrier recombination lifetime for alkali-substituted compounds, see Table 1, we infer that the lowest (highest) dark current for Rb (Na) determines the absolute value of the X-ray response in Figure 1b. We note that Rb^+ promotes the passivation of defects, whose existence has been confirmed already in $Cs_2AgBiBr_6$,[8] evidenced by its lowest dark current, see Figure 1d inset. Measurements of the PL quantum

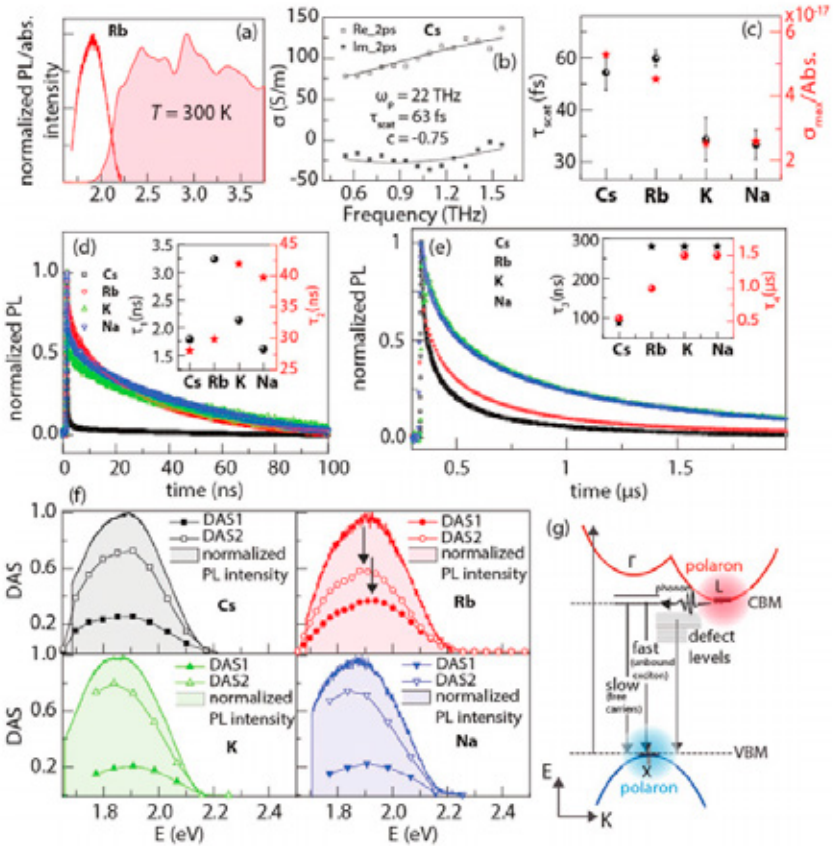

Figure **2.** Absorption, steady-state, and time-resolved PL and terahertz time-domain spectroscopy for $(Cs_{1-x}Y_x)_2AgBiBr_6$ single crystals/films. a) Absorption and PL spectra (λ_{exc} = 365 nm) for Rb at T = 300 K. b) Frequency-resolved THz conductivity at the pump–probe delay time of 2 ps on a film of compound Cs, fitted by the Drude–Smith model. c) Scattering time, τ_{scat}, averaged over several pump–probe delay times and photoconductivity maximum, σ_{max}, normalized to the absorbed photon density for all materials. d) PL lifetime (normalized decay signals) in the ns range recorded at the maximum steady-state PL. Upon alkali substitution, the carrier lifetime τ_2 is enhanced. The inset shows the extracted fast lifetimes τ_1 and τ_2 for all compounds. e) Fundamental carrier recombination lifetime (normalized decay signals) in the μs range recorded at the maximum steady-state PL. In general, the lifetimes increase upon alkali substitution in particular, the fundamental recombination lifetime τ_4 is enhanced. The inset shows the extracted longer lifetimes τ_3 and τ_4 for all compounds. f) Steady PL (filled area) and decay associated spectra (DAS, line + symbols) related to τ_3 (full symbols) and τ_4 (open symbols) recorded at various emission wavelengths for all compounds. Compound Rb shows a distinct behavior, indicated by the arrows. g) Proposed mechanism for the photo-physical pathways in these materials.

yield confirm higher values for Rb and Cs (≈1%) compared to K and Na (0.1–0.3%) indicating that the main recombination pathways are nonradiative, in particular, in the case of K and Na. Thus far, the results highlight that alkali substituted $Cs_2AgBiBr_6$ provides new avenues toward highly sensitive X-ray photodetectors. Already, double perovskites have shown the lowest detectable dose rate of 59.7 nGy_{air} s^{-1} in $Cs_2AgBiBr_6$ comparable to that of 55 nGy_{air} s^{-1} for $MAPbBr_3$[11] which is more than two orders of magnitude smaller compared to the lowest detectable dose rate in silicon, 8300 nGy_{air} s^{-1}.[24] A comparison based on the sensitivity between our materials and those of conventional X-ray detectors has been provided in the Supporting Information.

In the following, we determine the photo-physical properties in the UV/vis region and search for possible changes in the electronic states due to alkali-substitution. An example of the steady-state absorption and PL for Rb in the visible range at 300 K is shown in Figure 2a. The results for the other compounds measured at 300 and 77 K, are presented in Figure S4, Supporting Information. We note that the absorption spectra of all materials exhibit several "dips" above the band edge. Among them, the strongest one is found at 2.8 eV (marked with an asterisk) which becomes even more pronounced at 77 K. The origin of this minimum in the absorption spectrum is currently under debate and may be attributed to either a direct-bandgap exciton at the Γ point,[25] a defect-related directly bound exciton[26] or a metal-centered (e.g., Bi^{3+}) s–p orbital transition.[27] K and Na exhibit a slightly stronger dip at 2.8 eV compared to Cs and Rb. The absorption onsets at 300 K are fitted to the functional form $(E - E_g)^2$, which is the most accurate measure of the bandgap. We

extract an indirect E_g of (1.79 ± 0.02) eV (Cs), (1.86 ± 0.10) eV (Rb), (1.75 ± 0.10) eV (K), and (1.83 ± 0.08) eV (Na) where the error bars represent upper and lower limit of the bandgap extracted from a fitting range analysis. Small changes are detected in the absorption–emission landscape of Rb compared to the other compounds that are apparent in the excitation–emission maps at 77 K (see Figure S5, Supporting Information). The center of the normalized PL peak is found to be at 1.8 eV for all materials.

Next, the dynamics of the photoexcited charge carriers are addressed. To evaluate the role of alkali substitution on the electrical transport properties, more specifically the charge scattering time, τ_{scat}, and mobility, μ, we performed contact-free THz photoconductivity measurements in transmission with sub-ps time resolution on thin films of all samples (for film preparation see the Supporting Information). Note that large single crystals have been used for all measurements performed in this study except for THz photoconductivity measurements. In these measurements, the perovskite film is excited by a short laser pulse with a photon energy of ≈3.1 eV and a duration of 50 fs to create charge carriers (Figure S6b, Supporting Information), after which the photoconductivity spectrum (between 0.2 and 2.0 THz) is measured,[28] details see Experimental Section and Supporting Information. The photoinduced conductivity for all samples is represented in Figure S6d, Supporting Information. To determine τ_{scat} and μ, we conducted systematic frequency-resolved THz conductivity measurements for all four samples following photoexcitation, see Figure 2b as an example for Cs. Similar data of other compounds are shown in Figure S6e–h. We found that the Drude model, commonly used for describing the transport of charge carriers in semiconductors, is not applicable for our systems. The data sets are rather described best using the Drude–Smith model where backscattering of the charge carriers is also considered (details see the Supporting Information).[29–32] The average values of τ over the series of pump–probe delay times are presented in Figure 2c for all samples and we find τ_{scat} (Cs) ≈ τ_{scat} (Rb) > τ_{scat} (K) ≈ τ_{scat} (Na). From these values, we calculate $\mu = e \times \tau_{scat}/m^*$, where $m^* = 0.35m_0$[33] is the effective mass of electrons in units of electron mass m_0, which we assume to be the same for all materials and e is the elementary charge. We find $\mu \approx 100\ cm^2\ V^{-1}\ s^{-1}$ for $Cs_2AgBiBr_6$ emphasizing that this value represents the intrinsic, upper limit of μ as charge carriers are locally driven by the oscillating THz field (within a distance of around 10 nm) while the contribution of scattering at the boundaries and/or contacts can be excluded. The zero-frequency, long-range mobility for the thin film is calculated to be $\mu_{thin\text{-}film} \approx 30\ cm^2\ V^{-1}\ s^{-1}$, given the value for the averaged Drude-Smith c-parameter of −0.70 ($\mu_{thin\text{-}film} = \mu(1 + c)$). In addition, we applied a complementary approach[34,35] to estimate the lower limit for the mobility. This results in $\mu_{thin\text{-}film} > 2.6\ cm^2\ V^{-1}\ s^{-1}$, consistent with previous reports[34,36,37] and mobility values inferred from our fittings. The materials' photoconductivity, $\sigma = N_c e \mu$ where N_c is carrier density, is shown in Figure S6d, Supporting Information for all samples. σ_{max} normalized to the absorption is shown in Figure 2c for all materials.

The dynamics of the photogenerated charge carriers for all single crystals in the UV/vis range were investigated via transient PL measurements at T = 300 K over a range of detection wavelengths and timescales (ns to μs). Figure 2d illustrates the fast-decay processes (ns) recorded at the maximum of the steady-state PL under the excitation of 488 nm (2 μJ mm^{-2}). The luminescence decay times τ_n (n = 1, 2) are extracted using a sum of two exponentials. The extracted decay constants τ_1 ranging from 1 to 5 ns and τ_2 ranging from 25 to 45 ns, likely originate from excitons bound to traps and/or surface-states and free excitons, respectively.[10] The decay constant τ_2 for the alkali-substituted materials is enhanced as shown in the inset to Figure 2d. We note that the fast decay times (ns) are insensitive to the detection wavelength window.

The longer timescales (ns–μs) of the charge carriers under 450 nm excitation, shown for the maximum steady-state PL in Figure 2e as an example, are further elucidated within the framework of their relative decay associated spectra (DAS) in Figure 2f. The PL decay spectra for all compounds and all detection wavelength windows are presented in Figure S7, Supporting Information. Two distinct decay channels describe the spectra: DAS1 related to τ_3 peaks at energies slightly above the conduction band minimum (CBM) (full symbols), attributed to the intrinsic defect levels.[8,33] DAS2, associated to τ_4, peaks closest to the steady-state PL peak energy (open symbol), is attributed to a band-to-band radiative recombination.[9] τ_4, the material's fundamental recombination lifetime is enhanced up to a factor of three for alkali-substituted materials compared to $Cs_2AgBiBr_6$ (inset to Figure 2e). The high mobility and long recombination lifetime in combination with the so-called "giant" electron–phonon coupling reported for Cs,[9] and polar nature of the metal halide framework and its deformability suggests the presence of polarons in our system, as recently debated in halide perovskites.[38–40] In contrast to 2D halide perovskites in which small polarons form as a result of lattice confinement,[41] in 3D perovskites, the extent of lattice deformation as a result of electron–phonon interaction is limited by the topological constraints (keeping the electronic energy and the lattice elastic energy balanced). Hence, it has been proposed that large polarons may form spanning over a few lattice sites.[42] While polaron transport is described by band-like conduction of quasi-particles with an enhanced effective mass that limits the carrier mobility,[43] it has also been shown that large polarons are weakly scattered by phonons compensating their large momentum leading to mobilities.[44] We hypothesize that carrier transport is affected by polaron formation supported by temperature-dependent measurements of the carrier scattering time (mobility) for $Cs_2AgBiBr_6$ that scale as $\tau_{scat} \approx T^{-0.5}$ between 150 and 300 K, typical for transport dominated by large polarons[43] (Figure S8, Supporting Information).

Finally, we summarize our findings in a simplified sketch in Figure 2g showing the photo-physical processes of the systems under study including the polaron concept. Note, that in our model, the PL is based on band-to-band recombination following ref. [9]. In literature, the exact PL mechanism in Cs is still under debate.[25] The fast processes (ns lifetimes) are attributed to bound (to traps) and free excitons while the μs lifetime fits to the "slow" free carrier recombination processes. The phonons are assumed to align the momentum of a decaying electron in the CBM and a hole in the VBM. The different recombination pathways are separated in k-space for clarity.

At this point, it is not yet clear how atomic substitution affects the electron–phonon interaction. To evaluate the extent

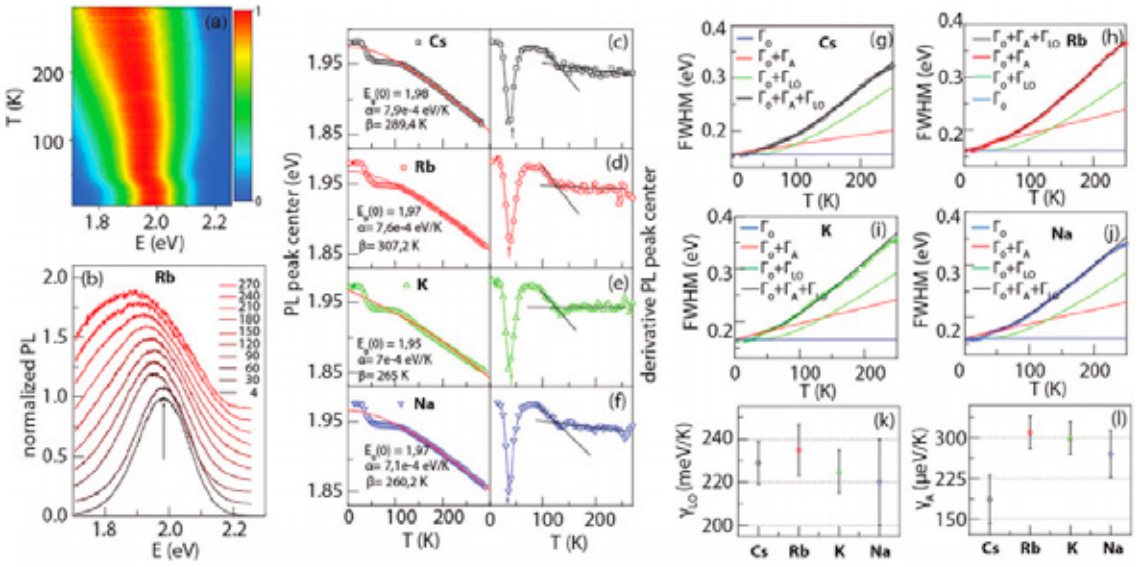

Figure 3. Temperature-dependent photoluminescence of single crystals $(Cs_{1-x}Y_x)_2AgBiBr_6$. a,b) 2D false color and waterfall plot of the PL as a function of several chosen temperatures from 300 to 4.2 K for Rb. c–f) (left) Extracted PL center c_x as a function of T for all materials: the straight line indicates a fit to the Varshni equation for conventional semiconductors (parameters see Table 1). Below 70 K, a sudden blueshift is found for all materials. (right) First derivative of the PL center indicating the changes of PL peak center as a function of T. The arrows indicate the maximum slope of the blueshift. The lines indicate change in the PL peak center around 125 K for all materials. g–j) Temperature dependence of emission linewidths for all materials: FWHM of the PL peak as a function of temperature for all compounds. The solid lines indicate the contributions to the line width broadening using Equation (1). k,l) Contributions of the optical and acoustic phonon scattering to the total linewidth for all materials.

of the crystal's electron–phonon interaction, we performed temperature-dependent steady-state PL in 5 K steps between 4.2 and 300 K. Figure 3a,b show the temperature evolution of the PL emission for Rb under 365 nm excitation represented in a 2D false color plot (a) and selected spectra (b) for the temperature range measured. The arrow indicates the peak center. For each temperature, the center of the PL peak has been determined via a Gaussian approximation and plotted in Figure 3c–f for all compounds. The PL exhibits a clear blueshift with decreasing temperature down to 4.2 K, corresponding to an increase in the bandgap reminiscent of conventional semiconductors and in contrast to organic lead-based perovskites. Below 70 K, the PL peak center is subject to a sudden, material dependent blueshift which saturates below 25 K. For better illustration, the derivative of the peak center is plotted as a function of T in Figure 3c–f on the right side. The arrows indicate the blueshift and the crossing of the solid lines indicate the structural phase transition temperature as discussed in detail later. For the high-temperature data (100–280 K), we fit the PL peak center to the Varshni empirical expression $E_g(T) = E_g(0) - \alpha T^2/(T+\beta)$ that accounts for the temperature dependence of the bandgap to a first approximation and in the absence of defect luminescence. $E_g(0)$ is the gap at zero-temperature, and α and β are material constants where β has the dimension of temperature and is related to the Debye temperature via a coefficient.[45] The extracted $E_g(0)$ for $Cs_2AgBiBr_6$ agrees with the value extracted from an absorption experiment at 25 K.[10] The extracted parameters are listed in each figure, respectively (Figure 3c–f).

To unveil the different scattering mechanisms that charge carriers are subject to, we analyze the temperature evolution of the emission line widths (full-width at half maximum (FWHM)) extracted from the Gaussian fits at different temperatures for $(Cs_{1-x}Y_x)_2AgBiBr_6$ shown as a function of temperature in Figure 3g–j for all compounds. For all materials, we have performed a fit based on the total PL broadening $\Gamma(T)$ being described as follows.[46]

$$\Gamma(T) = \Gamma_0 + \Gamma_A + \Gamma_{LO} = \Gamma_0 + \gamma_A T + \gamma_{LO} n(T) \quad (1)$$

where Γ_0 is the zero-temperature line width, Γ_A and Γ_{LO} represent the temperature-dependent acoustic and optical carrier–phonon scattering contributions with their coupling constants γ_A and γ_{LO}, respectively. $n(T) = \frac{1}{e^{\frac{\hbar\omega_0}{k_B T}} - 1}$ is the Bose–Einstein distribution function. $\hbar\omega_0 = 22$ meV as found from previous Raman measurements [9] and is considered to be the same for all compounds as the substitution is only 2% and no differences in their Raman spectra were observed at room temperature. The resulting coupling constants are presented in Figure 3k,l and Table 1. To determine the different contributions of acoustic and optical phonon scattering in our materials, the following procedure has been employed. First, we assess γ_A via a linear fit ($\Gamma_0 + \gamma_A T$) in the low-temperature regime where the acoustic phonon scattering is expected to be the dominant contribution. However, in the presence of the anomalous "transition" related to a structural change in the material below 50 K and given the

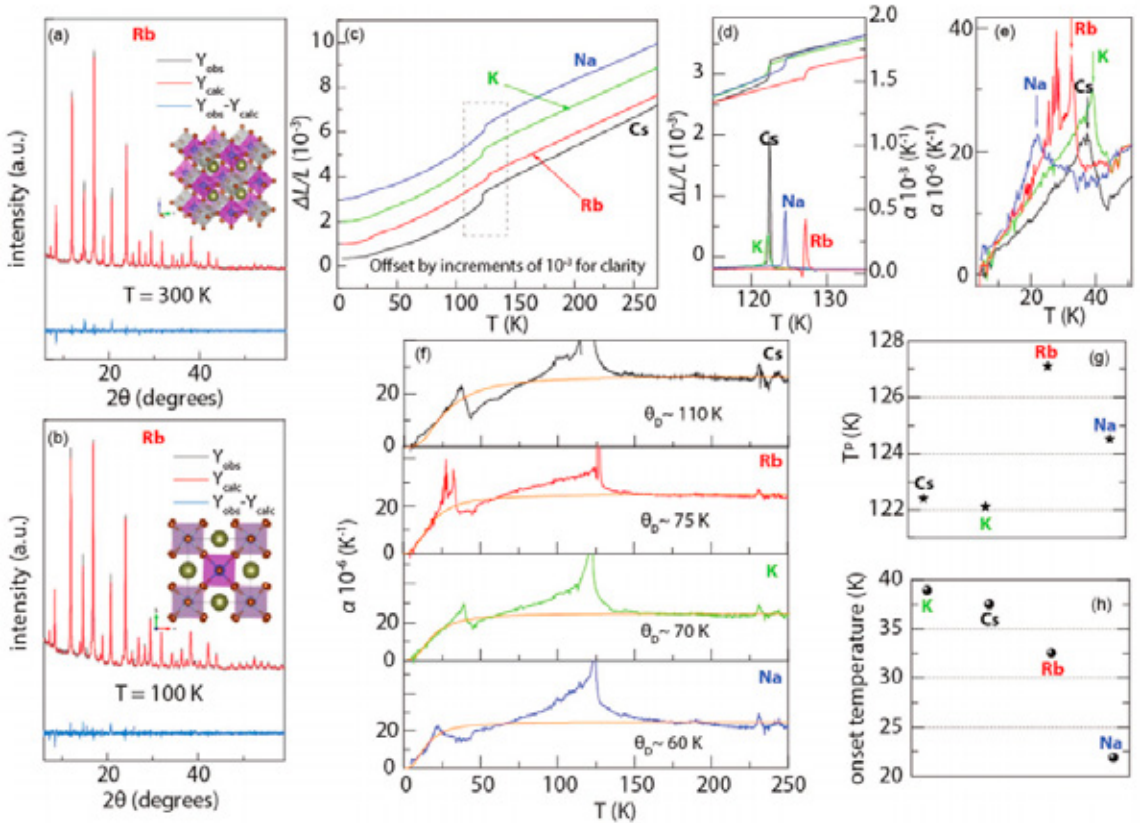

Figure 4. XRD diffraction, structural phase transitions and thermal expansion coefficient for all materials. a,b) XRD diffraction patterns and corresponding Bragg peak locations at 300 and 100 K for $(Cs_{1-x}Rb_x)_2AgBiBr_6$. c) Linear thermal expansion $\Delta L/L$ for all compounds (the curves are offset for clarity by 1×10^{-3}). The gray dashed box indicates the structural phase transition from a high-temperature cubic to a low-temperature tetragonal phase. d) $\Delta L/L$ and α in the T range where the structural phase transitions occur (122 and 128 K). e) α at low temperatures for all materials: the thermal expansion coefficient is found to show a material-dependent upturn below 50 K. The arrows indicate structural anomalies at lower temperatures. f) Thermal expansion coefficient α for $Cs_2AgBiBr_6$ and the alkali metal substituted compounds. The solid line is a fit to the Debye model. g) Phase transition temperature for all materials between 122 and 128 K. h) Maximum of α for all materials as indicated by the arrows in (e) that corresponds to a sudden blueshift as found in the PL data.

limited number of points available, we only obtain an upper limit for γ_A. Then, we perform a fit using Equation (1). The individual contributions to the total PL broadening $\Gamma(T)$ are plotted in Figure 3g–i. While the low-temperature regime is governed by acoustic phonon scattering, the high-temperature regime is dominated by longitudinal optical (LO) phonon scattering as is the case for lead-halide perovskites and double perovskites.[9,46] We find that γ_{LO} remains constant within the error bars for all materials while γ_A shows an increase for the alkali-substituted materials hinting to a "softer" crystal structure as demonstrated through the octahedral distortion parameter and instability factor in the XRD analysis (see Supporting Information).

To assess their structural properties upon atomic substitution, we now look into the temperature evolution of the compounds by means of high-resolution PXRD and thermal expansion. All single crystals were characterized and indexed via high-resolution PXRD at 300 and 100 K, shown for Rb in Figure 4a,b respectively. The results for the other materials are presented in Figure S1, Supporting Information. At 300 K, the crystal structure is defined with the cubic structure of the mother compound consisting of alternating $BiBr_6$ and $AgBr_6$ octahedra[47] (Figure 4a) whereas at 100 K significant asymmetric peak broadening was observed indicating a second-order phase transition from Fm-3m to I4/m. This is consistent with an out-of-phase tilt of the octahedral framework based on group-theoretical analysis of the ideal cubic double perovskite,[48] described by $a^0a^0c^-$ in Glazer's notation.[10,49] The asymmetric shape of the peaks was successfully described with Rietveld refinement (Figure 4b).

The linear thermal expansion $\Delta L/L$ and thermal expansion coefficient α have been measured during an adiabatic warm-up to 260 K using a capacitive dilatometer.[50] Figure 4c shows $\Delta L/L$ in the entire temperature range for all compounds as indicated. The dashed gray box indicates the phase transition from a tetragonal low-temperature to a cubic high-temperature phase as found in XRD experiments for $Cs_2AgBiBr_6$.[10] $\Delta L/L$ is

positive with the same magnitude for all compounds, yet, above the phase transition temperature T^P, $\Delta L/L \propto T$ in contrast to the methylammonium-based lead halide materials.[51] Both $\Delta L/L$ and α are illustrated for the temperature region in the vicinity of the structural phase transition temperature in Figure 4d. The T^Ps are summarized in Figure 4g for all materials extracted from the maximum of α. For Cs, we find T^P = 122.5 K, in agreement with ref. [10] showing the strongest transition in $\Delta L/L$ among all compounds under study. Alkali substitution has a severe impact on the phase transition temperatures. While for Na and Rb, T^P is found to increase by a few degrees kelvin, K exhibits a slightly lower phase transition temperature compared to $Cs_2AgBiBr_6$. We note that apart from the phase transition seen as a cusp-like feature in α, we observe an anomaly in the thermal expansion coefficient below 50 K that has neither been found in XRD nor in measurements of the specific heat.[10] This anomaly is highlighted in an extended range in Figure 4e with the maxima indicated by arrows for each material. The maximum of this anomaly (maximum of α) for all samples is shown in Figure 4h showing an opposite trend compared to T^P. Since the blueshift found in the PL for all the materials occurs in the same temperature range, we relate this blueshift to most likely a structural anomaly in the materials whose origin is yet to be determined by, for example, low T XRD. We suggest that the observed variations in T^P within ΔT = 6 K upon alkali-substitution are related to the global instability index, GII, calculated from PXRD indicating the amount of strain in the materials. While significant strain is found in the cubic phase due to the relatively low valence of alkali atoms, smaller GII values have been obtained in the tetragonal phase indicating a reduced strain.

The overall temperature dependence of α follows the Debye model, which is a measure of the contribution of acoustic phonons to the specific heat.[52] The Debye model adapted to the thermal expansion coefficient[53] reads:

$$\alpha(T) = \alpha(0)\left(\frac{T}{\Theta_D}\right)^3 \int_0^{\Theta_D/T} \frac{x^4 e^x dx}{(e^x - 1)^2} \quad (2)$$

where $\alpha(0)$ is a temperature-independent fitting parameter and Θ_D is the Debye temperature defined as the material-specific temperature at which all acoustic phonon modes are thermally excited. The overall dependence of α, see Figure 4f, follows the Debye model, excluding the region of the low-temperature anomaly and the structural phase transition. The estimated values for the Debye temperature for all materials are summarized in Table 1. Θ_D for Cs is in agreement with measurements of the specific heat[10] and Θ_D decreases for the alkali-substituted compounds suggesting a slightly "softer" structure confirmed by the enhanced acoustic phonon coupling constants and octahedral distortion parameter and instability factor calculated from the XRD analysis (details see the Supporting Information).

To conclude, we have demonstrated that alkali substitution of Cs^+ in $Cs_2AgBiBr_6$ by Na^+, K^+, and Rb^+ has a severe impact on the response to high energy radiation and the structural phase transition temperature. While the size and indirect nature of the bandgap are not altered upon alkali substitution, the PL linewidth analysis reveals enhanced electron-acoustic phonon coupling. The overall change in the X-ray response, we attribute to changes in the charge transport properties in highly stable double perovskites including high mobility, longer fundamental recombination lifetime, different dark currents and likely polaron formation as a result of strong optical electron–phonon coupling. Our results suggest the possibility to ultimately employ cation substitution as tuning parameter of the intrinsic material properties toward a new material platform for optoelectronic devices.

Experimental Section

Growth of Single Crystals: $Cs_2AgBiBr_6$ was grown according to the procedure reported by Slavney et al.[5] A mixture of 1.0 mmol of $BiBr_3$ (≥98%, Sigma-Aldrich) and 2.0 mmol of CsBr (99.9%, Sigma-Aldrich) in 10 mL of HBr (≥99.99%, 48 w%, Honeywell Fluka) in a 40 mL vial was sonicated for 5 min. After adding 1.0 mmol AgBr (≥99%, Chem-Lab), the suspension was sonicated for 5 min and then heated to 120 °C to obtain a supersaturated solution. The mixture was cooled according to the following protocol:

First, it was kept at 120 °C for 3 h, then cooled by 2 °C h^{-1} to 100 °C, and further by lower cooling rate of 1 °C h^{-1} to 50 °C. After that, mm-sized single crystals could be collected from the mixture by filtration. The crystals were washed with isopropanol (HPLC grade, Sigma-Aldrich) and then dried in a vacuum oven at 60 °C. The synthesis was performed under ambient atmospheric conditions.

Given the higher solubility of the NaBr, KBr, and RbBr salts in HBr, slight changes were applied to the previously reported method for growing the alkali-substituted $Cs_2AgBiBr_6$ crystals,[5] that is, the process was initiated with a more concentrated precursor mixture and with an adjusted temperature profile. The precursor solution (1.05 mM) contained a 50:50 CsBr/Rb(K,Na)Br (99.9%, Sigma-Aldrich) molar ratio from which ultimately only 2% of the Cs was replaced by the alkali metal. It was observed that crystal nucleation occurred relatively fast, but crystal growth continued until lower temperatures. In order to fulfill the complete process of crystal formation, the temperature profile was slightly adjusted. The temperature was kept for another 12 h at 50 °C and then an extra 1 °C h^{-1} cooling step to 40 °C was introduced.

UV–Vis Diffuse Reflectance Spectroscopy: Optical diffuse-reflectance data were recorded between 300 and 800 nm with a step of 1 nm via PerkinElmer Lambda 950 UV–vis spectrophotometer equipped with an integrating sphere at ambient temperature. $BaSO_4$ powder was used as reference. The diffused reflectance (R) was converted to F(R) using the Kubelka–Munk function: $F(R) = (1 - R)^2/2R$.

Low-Temperature PL Spectroscopy: A He flow cryostat in which the temperature can be varied from 4.2 to 300 K was used to measure low T PL. The sample was mounted on an insert and was excited with a solid-state laser (Thorlabs M365LP1 with driver DC2200) operating at 365 nm via a 550 µm core optical fiber. The PL spectra were collected through 11 optical fibers with a core of 200 µm surrounding the excitation fiber in an increment of 5 K. The fibers were coupled to a LOT-QD Shamrock F/4 spectrometer with an electron-multiplying charge-coupled detector iXon DV887.

Time-Resolved Luminescence Spectroscopy: The recorded emission lifetimes, across all time-resolved methods, were the superposition of multiple radiative transitions. All the decay spectra in the main text were analyzed using a sum of the exponential decays of multiple decaying components, with differing decay constants (τ_j) and DAS[54] amplitudes ($C_j(\lambda)$). The decay times have been extracted using the following relation considering the time of excitation (t_0).

$$I_e(\lambda,t) = \sum f_j(\lambda,\tau_j) = \sum_j (\lambda)\, e^{-(t-t_0/\tau_j)} \quad (3)$$

where $f(\lambda,\tau_j)$ is the deconvolved total fluorescence at wavelength λ at time t after the excitation pulse. The amplitude C_j of each decaying

component species, τ_j, as a function of the emission wavelength, λ, constitute the so-called DAS in the main text.

PL emission lifetime Experiments: Samples were systematically excited using a pulsed Nd:YAG laser (Quanta-Ray INDI-40, Spectra Physics) and an optical parametric oscillator (355, 406, and 488 nm wavelengths). The excitation wavelength was fixed at 450 nm and a fluence of 1.7 μJ mm^{-2}. The pulse duration was estimated to 8 ns and the time resolution of the experiment was about 10 ns. The excitation light was focused on the sample through a lens (f ≈ 300 mm). To generate a trigger signal, a small part of the excitation light was sent to a fast photodiode. Emission signals were collected, filtered, and focused on the entrance slit of a 30 cm focal length spectrograph (SpectroPro-300i Acton) in a right-angle configuration. The detector was a photomultiplier tube (Hamamatsu, R928) and the transient electrical signal was displayed by an oscilloscope connected to the control computer. A homemade Labview-based software was used to control and trigger the instruments, read, average, and store the transient data.

Device Fabrication: All bulk single crystals with flat facets up to 4 × 4 mm^2 and a thickness of 2 mm were used with a vertical structure of Au/crystal/Au using Au as the ohmic contact for the X-ray sensitivity tests.

X-ray Detection Device Characterization: During the experiments, the devices in the configuration of Au/double-perovskite single crystal/Au were exposed to a tungsten anode X-ray tube (maximum X-ray photon energy 70 keV, peak intensity 30 keV). By changing the current of the X-ray tube, precise control over the X-ray dose was achieved while the distance between the source and the device was kept constant.

The X-ray spot size was about 3 mm. The device was placed into a liquid nitrogen based Linkam temperature stage (THMS600 Linkam stage, Variable Temperature between 80 and 500 K) for measurements. A Keithley 2000 was used to apply the bias voltage and record the response current. The X-ray dose rate was tuned via varying the operational current and using different thicknesses of Al foil between the source and crystals. The X-ray dose rate was carefully calibrated with a RaySafe Model Solo R/F dosimeter. The temperatures were varied from 100 to 280 K. All the X-ray response characterization was conducted in the dark.

Thermal Expansion Experiments: Thermal expansion measurements were carried out using a high-resolution capacitive dilatometer.[50] The dilatometer was fixed on a probe, put into a vacuum tube with a sufficient amount of ^{4}He contact gas that has been added before the experiment to ensure thermal equilibrium. All materials with a thickness L of 1 to 2 mm have been cooled down to 4.2 K and Thermal expansion has been measured during the warm-up (with a maximum warm up time of 72 h) to ensure quasi-adiabatic conditions. The length change ΔL of the sample along the main axis was measured using an ultrahigh-resolution Andeen–Hagerling capacitance bridge (AH2500).

Terahertz Photoconductivity Measurements: This technique provides a contact-free means for photoconductivity measurements. Using an ultrashort visible laser pulse (400 nm, FWHM ≈ 50 fs), charge carriers were optically injected into the conduction bands. Subsequently, the conductivity of the photogenerated charge carrier was probed by freely propagating single-cycle THz electromagnetic transients with 1–2 ps duration. The quickly oscillating terahertz field E(t) accelerated the charges, which, in turn, modifies the terahertz pulse. The relative modification $-\Delta E/E(t)$ of the THz field can be directly measured and related to the photoconductivity σ. The analysis was typically performed in the frequency domain by Fourier transformation, that is, $\sigma(\omega) \approx -\Delta E/E(\omega)$. The photoconductivity as a function of time delay t_d between excitation and THz pulse $\sigma(\omega,t_d)$ was a complex value, and its real part, $\mathrm{Re}[\sigma(\omega,t_d)]$, corresponding to the changes in the peak intensity of THz pulse following photoexcitation, was directly related to the macroscopic transport parameters in electrical measurements, by $\mathrm{Re}[\sigma(\omega; t_d)] = N_{pump} \times e \times \mu(\omega; t_d)$ where N_{pump} and $\mu(\omega; t_d)$ were the time-dependent carrier density and mobility following photoexcitation, respectively. Terahertz spectroscopy thus provides information on charge carrier dynamics on a timescale complementary to that obtained using time-resolved PL measurements (sub-ps versus ns).

Fluorescence Lifetime Imaging: A pulsed white light laser (SuperK Extreme EXW-12, NKT Photonics) operating at 488 nm and set at a repetition rate of 10 MHz and a fluence of 2 μJ mm^{-2} was employed as excitation source. The excitation laser beam was directed into the crystals through an oil immersion objective (HCPLAPO 100 × 1.4 NA) of an inverted microscope system (Leica DMi8). The fluorescence photons were detected by an avalanche photodiode (SPCM-AQR-14, Perkin–Elmer) via the same objective filtered by the main dichroic and cut-off filters. Photon counting and time tagging were performed within a TimeHarp 200 module (PicoQuant), with a time resolution of 29 ps per channel. The FLIM images were analyzed using SymphoTime 32 software (PicoQuant).

Temperature-Dependent PXRD Measurements: High-resolution, temperature-dependent measurements were performed at the Diamond Light Source, beamline I11.[55] Measurements were performed on all samples at room temperature and 100 K at a wavelength of 0.825 Å with an Oxford Cryosystems Cryostream Plus 700 device and cooled at 360 K h^{-1}. Samples were ground to fine powders, mixed with amorphous boron to reduce X-ray absorption and loaded in 0.3 mm diameter borosilicate capillaries. Rietveld analysis was performed using the FullProf suite.[56]

Supporting Information

Supporting Information is available from the Wiley Online Library or from the author.

Acknowledgements

The authors acknowledge financial support from the Research Foundation-Flanders (FWO, Grant Nos. G.0962.13, 1203719N and 12Y6418N, postdoctoral fellowship to J.S., E.D., and M.K., FWO project G098319N to M.K. and "Krediet aan Navorsers" 1514220N), the Flemish government through long-term structural funding Methusalem (CASAS2, Meth/15/04), the Hercules Foundation (HER/11/14), the Belgian Federal Science Policy Office (IAP-PH05), KU Leuven (C14/19/079), and the EC through the Marie Curie ITN project iSwitch (GA-642196). The support of the HFML-RU/FOM, member of the European Magnetic Field Laboratory (EMFL), is also acknowledged. The authors thank Diamond Light Source Ltd. for access to beamline I11 (proposal CY22020-1). Chiu Tang, Sarah Day, and Laura Wollesen are thanked for their assistance with the measurements. M.O. and M.B. gratefully acknowledge funding from the Danish Council for Independent Research under the Sapere Aude program (7027-00077B) and VILLUM FONDEN via the Centre of Excellence for Dirac Materials (11744). R.K. is supported by the German Science Foundation through Project No. KU 3287/1-1. The authors acknowledge the help and support from Luc Struye and Dirk Vandenbroucke from AGFA NV, Innovation Office/Technology & Innovation, Septestraat 27, 2640 Mortsel, Belgium, where all X-ray sensitivity tests were performed. The authors are grateful to Prof. Vanacken for the support with the low temperature PL measurements.

Open access funding enabled and organized by Projekt DEAL.

Conflict of Interest

The authors declare no conflict of interest.

Keywords

alkali-substitution, double perovskites, electron–phonon coupling, photophysical properties, X-ray response

Received: March 18, 2020
Revised: July 12, 2020
Published online: August 31, 2020

[1] W. Ke, C. C. Stoumpos, M. G. Kanatzidis, Adv. Mater. **2019**, *31*, 1803230.
[2] E. Greul, M. L. Petrus, A. Binek, P. Docampo, T. Bein, J. Mater. Chem. A **2017**, *5*, 19972.
[3] C. Wu, Q. Zhang, Y. Liu, W. Luo, X. Guo, Z. Huang, H. Ting, W. Sun, X. Zhong, S. Wei, S. Wang, Z. Chen, L. Xiao, Adv. Sci. **2018**, *5*, 1700759.
[4] G. Volonakis, M. R. Filip, A. A. Haghighirad, N. Sakai, B. Wenger, H. J. Snaith, F. Giustino, J. Phys. Chem. Lett. **2016**, *7*, 1254.
[5] A. H. Slavney, T. Hu, A. M. Lindenberg, H. I. Karunadasa, J. Am. Chem. Soc. **2016**, *138*, 2138.
[6] R. L. Z. Hoye, L. Eyre, F. Wei, F. Brivio, A. Sadhanala, S. Sun, W. Li, K. H. L. Zhang, J. L. Macmanus-Driscoll, P. D. Bristowe, R. H. Friend, A. K. Cheetham, F. Deschler, Adv. Mater. Interfaces **2018**, *5*, 1800464.
[7] D. Bartesaghi, A. H. Slavney, M. C. Gélvez-Rueda, B. A. Connor, F. C. Grozema, H. I. Karunadasa, T. J. Savenije, J. Phys. Chem. C **2018**, *122*, 4809.
[8] J. A. Steele, W. Pan, C. Martin, M. Keshavarz, E. Debroye, H. Yuan, S. Banerjee, E. Fron, D. Jonckheere, C. W. Kim, W. Baekelant, G. Niu, J. Tang, J. Vanacken, M. Van Der Auweraer, J. Hofkens, M. B. J. Roeffaers, Adv. Mater. **2018**, *30*, 1870353.
[9] J. A. Steele, P. Puech, M. Keshavarz, R. Yang, S. Banerjee, E. Debroye, C. W. Kim, H. Yuan, N. Ho Heo, J. Vanacken, A. Walsh, J. Hofkens, M. B. J. Roeffaers, ACS Nano **2018**, *12*, 8081.
[10] L. Schade, A. D. Wright, R. D. Johnson, M. Dollmann, B. Wenger, P. K. Nayak, D. Prabhakaran, L. M. Herz, R. Nicholas, H. J. Snaith, P. G. Radaelli, ACS Energy Lett. **2019**, *4*, 299.
[11] W. C. Pan, H. Wu, J. Luo, Z. Deng, C. Ge, C. Chen, X. Jiang, W.-J. Yin, G. Niu, L. Zhu, L. Yin, Y. Zhou, Q. Xie, X. Ke, M. Sui, J. Tang, Nat. Photonics **2017**, *11*, 726.
[12] B. Yang, W. Pan, H. Wu, G. Niu, J.-H. Yuan, K.-H. Xue, L. Yin, X. Du, X.-S. Miao, X. Yang, Q. Xie, J. Tang, Nat. Commun. **2019**, *10*, 1989.
[13] T. Sato, S. Takagi, S. Deledda, B. C. Hauback, S. Orimo, Sci. Rep. **2016**, *6*, 23592.
[14] K. Y. Tsui, N. Onishi, R. F. Berger, J. Phys. Chem. C **2016**, *120*, 23293.
[15] J. P. Correa-Baena, Y. Luo, T. M. Brenner, J. Snaider, S. Sun, X. Li, M. A. Jensen, N. T. P. Hartono, L. Nienhaus, S. Wieghold, J. R. Poindexter, S. Wang, Y. S. Meng, Ti Wang, B. Lai, M. V. Holt, Z. Cai, M. G. Bawendi, L. Huang, T. Buonassisi, D. P. Fenning, Science **2019**, *363*, 627.
[16] M. Saliba, T. Matsui, K. Domanski, J.-Y. Seo, A. Ummadisingu, S. M. Zakeeruddin, J.-P. Correa-Baena, W. R. Tress, A. Abate, A. Hagfeldt, M. Gratzel, Science **2016**, *354*, 206.
[17] M. Saliba, T. Matsui, Ji-Y Seo, K. Domanski, J.-P. Correa-Baena, M. K. Nazeeruddin, S. M. Zakeeruddin, W. Tress, A. Abate, A. Hagfeldt, M. Grätzel, Energy Environ. Sci. **2016**, *9*, 1989.
[18] M. Zhang, J. S. Yun, Q. Ma, J. Zheng, C. F. J. Lau, X. Deng, J. Kim, D. Kim, J. Seidel, M. A. Green, S. Huang, A. W. Y. Ho-Baillie, ACS Energy Lett. **2017**, *2*, 438.
[19] T. Duong, Y. Wu, H. Shen, J. Peng, X. Fu, D. Jacobs, Er-C Wang, T. C. Kho, K. C. Fong, M. Stocks, E. Franklin, A. Blakers, N. Zin, K. Mcintosh, W. Li, Yi-B Cheng, T. P. White, K. Weber, K. Catchpole, Adv. Energy Mater. **2017**, *7*, 1700228.
[20] S. H. Turren-Cruz, M. Saliba, M. T. Mayer, H. Juárez-Santiesteban, X. Mathew, L. Nienhaus, W. Tress, M. P. Erodici, M.-J. Sher, M. G. Bawendi, M. Grätzel, A. Abate, A. Hagfeldt, J.-P. Correa-Baena, Energy Environ. Sci. **2018**, *11*, 78.
[21] M. Abdi-Jalebi, Z. Andaji-Garmaroudi, S. Cacovich, C. Stavrakas, B. Philippe, J. M. Richter, M. Alsari, E. P. Booker, E. M. Hutter, A. J. Pearson, S. Lilliu, T. J. Savenije, H. Rensmo, G. Divitini, C. Ducati, R. H. Friend, S. D. Stranks, Nature **2018**, *555*, 497.
[22] J. W. Lee, D. J. Seol, A. N. Cho, N. G. Park, Adv. Mater. **2014**, *26*, 4991.
[23] D. J. Kubicki, D. Prochowicz, A. Hofstetter, S. M. Zakeeruddin, M. Grätzel, L. Emsley, J. Am. Chem. Soc. **2017**, *139*, 14173.
[24] R. Su, W. B. Ma, Y. Yang, J. Semicond. **2020**, *41*, 051204.
[25] Zelewski, J. Mater. Chem. C **2019**, *7*, 8350.
[26] A. Dey, A. F. Richter, T. Debnath, H. Huang, L. Polavarapu, J. Feldmann, ACS Nano **2020**, *14*, 5855.
[27] Y. Bekenstein, J. C. Dahl, J. Huang, W. T. Osowiecki, J. K. Swabeck, E. M. Chan, P. Yang, A. P. Alivisatos, Nano Lett. **2018**, *18*, 3502.
[28] R. Ulbricht, E. Hendry, J. Shan, T. F. Heinz, M. Bonn, Rev. Mod. Phys. **2011**, *83*, 543.
[29] N. V. Smith, Phys. Rev. B **2001**, *64*, 155106.
[30] Z. Chen, H. I. Wang, J. Teyssandier, K. S. Mali, T. Dumslaff, I. Ivanov, W. Zhang, P. Ruffieux, R. Fasel, H. J. Räder, D. Turchinovich, S. De Feyter, X. Feng, M. Kläui, A. Narita, M. Bonn, K. Müllen, J. Am. Chem. Soc. **2017**, *139*, 3635.
[31] I. Ivanov, Y. Hu, S. Osella, U. Beser, H. I. Wang, D. Beljonne, A. Narita, K. Müllen, D. Turchinovich, M. Bonn, J. Am. Chem. Soc. **2017**, *139*, 7982.
[32] H.-J. Feng, W. Deng, K. Yang, J. Huang, X. C. Zeng, J. Phys. Chem. C **2017**, *121*, 4471.
[33] Z. Xiao, W. Meng, J. Wang, Y. Yan, ChemSusChem **2016**, *9*, 2628.
[34] G. Longo, S. Mahesh, L. R. V. Buizza, A. D. Wright, A. J. Ramadan, M. Abdi-Jalebi, P. K. Nayak, L. M. Herz, H. J. Snaith, ACS Energy Lett. **2020**, *5*, 2200.
[35] C. Wehrenfennig, G. E. Eperon, M. B. Johnston, H. J. Snaith, L. M. Herz, Adv. Mater. **2014**, *26*, 1584.
[36] D. Bartesaghi, A. H. Slavney, M. C. Gélvez-Rueda, B. A. Connor, F. C. Grozema, H. I. Karunadasa, T. J. Savenije, J. Phys. Chem. C **2018**, *122*, 4809.
[37] E. M. Hutter, M. C. Gélvez-Rueda, D. Bartesaghi, F. C. Grozema, T. J. Savenije, ACS Omega **2018**, *3*, 11655.
[38] D. W. deQuilettes, K. Frohna, D. Emin, T. Kirchartz, V. Bulovic, D. S. Ginger, S. D. Stranks, Chem. Rev. **2019**, *119*, 11007.
[39] X. Y. Zhu, V. Podzorov, J. Phys. Chem. Lett. **2015**, *6*, 4758.
[40] D. Ghosh, E. Welch, A. J. Neukirch, A. Zakhidov, S. Tretiak, J. Phys. Chem. Lett. **2020**, *11*, 3271.
[41] A. R. S. Kandada, C. Silva, arXiv:1908.03909, **2019**.
[42] F. Zheng, L. W. Wang, Energy Environ. Sci. **2019**, *12*, 1219.
[43] J. M. Frost, Phys. Rev. B **2017**, *96*, 195202.
[44] D. Emin, Polarons, Cambridge University Press, Cambridge **2012**.
[45] Y. P. Varshni, Physica **1967**, *34*, 149.
[46] A. D. Wright, C. Verdi, R. L. Milot, G. E. Eperon, M. A. Pérez-Osorio, H. J. Snaith, F. Giustino, M. B. Johnston, L. M. Herz, Nat. Commun. **2016**, *7*, 11755.
[47] E. T. McClure, M. R. Ball, W. Windl, P. M. Woodward, Chem. Mater. **2016**, *28*, 1348.
[48] C. J. Howard, B. J. Kennedy, P. M. Woodward, Acta Crystallogr. B **2003**, *59*, 463.
[49] A. M. Glazer, Acta Crystallogr. B **1972**, *28*, 3384.
[50] R. Kuchler, T. Bauer, M. Brando, F. Steglich, Rev. Sci. Instrum. **2012**, *83*, 095102.
[51] M. Keshavarz, M. Ottesen, S. Wiedmann, M. Wharmby, R. Küchler, H. Yuan, E. Debroye, J. A. Steele, J. Martens, N. E. Hussey, M. Bremholm, M. B. J. Roeffaers, J. Hofkens, Adv. Mater. **2019**, *31*, 1900521.
[52] N. W. Ashcroft, N. D. Mermin, Solid State Physics, Holt, Rinehart and Winston, New York **1976**.
[53] P. Dutta, D. Bhoi, A. Midya, N. Khan, P. Mandal, S. Shanmukharao Samatham, V. Ganesan, Appl. Phys. Lett. **2012**, *100*, 251912.
[54] J. E. Loefroth, J. Phys. Chem. **1986**, *90*, 1160.
[55] S. P. Thompson, J. E. Parker, J. Potter, T. P. Hill, A. Birt, T. M. Cobb, F. Yuan, C. C. Tang, Rev. Sci. Instrum. **2009**, *80*, 075107.
[56] J. Rodriguez-Carvajal, IUCr Newsl **2001**, 26.